ATMOSPHERIC LOSSES OF N + AND O + UNDER THE EXTREME SOLAR CONDITIONS DURING GEOMAGNETIC REVERSALS

©2025 O. Tsareva[a] , A. Cannell[b] , N. Levashov[a,c] , H. Malova[a,d] , V. Popov [a,c,e], and L. Zelenyi[a]

[a]Space Research Institute, Moscow, Russia
[b]Italian Institute of Human Paleontology (IsIPU), Rome, Italy
[c]Lomonosov MSU, Faculty of Physics, Moscow, Russia
[d]Scobeltsyn Institute of Nuclear Physics of Lomonosov MSU, Moscow, Russia
[e]National Research University "Higher School of Economics", Moscow, Russia
**e-mail: olga8.92@mail.ru*

Received October 23, 2023
Revised November 12, 2023
Accepted November 13, 2023

Abstract. According to the widespread concept, the magnetosphere shields the planet's atmosphere from erosion caused by the solar wind. We have previously shown that during geomagnetic polarity reversals, when the magnetic field weakens to about 10% of the present one, its shielding is still effective. This conclusion was obtained for quiet periods of solar activity. However, since the duration of a geomagnetic reversal can cover several thousand years, during which many extreme events can occur, changes in solar parameters such as solar wind pressure and EUV-flux should be considered. At high EUV-flux, the concentrations of nitrogen and oxygen, as well as their losses, increase in the Earth's upper atmosphere. We have considered the most significant mechanisms of heavy ion escape from Earth's atmosphere and estimated their losses within the framework of a semi-empirical model. The results show that a weak geomagnetic field and strong solar activity lead to a change in the dominant escape mechanism and to significant atmospheric losses of preferentially lighter isotopes.

Keywords: *geomagnetic reversal, ionospheric loss, Earth's atmospheric escape*

DOI: 10.31857/S00234206250106e2

INTRODUCTION

On Earth over the past 600 million years (this geological period is characterized by the emergence of multicellular life and is called the Phanerozoic), five mass extinctions of all species of living beings have occurred [1]. The last mass Cretaceous-Paleogene extinction about 65 million years ago, which affected about 75 % of all living organism species and included the extinction of non-avian dinosaurs, was not the most significant. The largest Permian extinction 252 million years ago destroyed 96 % of all marine species and 73 % of terrestrial vertebrate species [1]. The causes of these events are still being debated [2], in particular, external impacts are considered (for example, Earth's collision with an asteroid at the end of the Cretaceous period), major volcanic eruptions (in the late Permian and Triassic periods), global cooling or warming of the climate. Paleontological data show that four great Phanerozoic extinctions: Ordovician,

Devonian, Permian-Triassic, and Triassic-Jurassic [3] followed the polarity change of geomagnetic superchrons (intervals of fixed polarity of the geomagnetic field lasting several tens of millions of years) with a delay of approximately 10–20 million years after the end of each superchron.

Geomagnetic inversions occur chaotically and against the background of significant weakening of the magnetic field [4, 5]. According to the hypothesis [6], a weakened magnetic field cannot effectively protect the planet's atmosphere from dissipation under the influence of the solar wind (SW). Therefore, multiple inversions over millions of years, in principle, could lead to continuous loss of atmospheric oxygen and a significant drop in its level [7]. Another argument in favor of this hypothesis is the increase in the ratio of heavy isotopes to light ones during inversions (light isotopes evaporate more quickly) [8].

Figure 1 shows the frequency of inversions (a), the level / mass of oxygen (b), and the change in the ratio of nitrogen isotopes (c) during the Phanerozoic era (0–550 million years ago; the count starts from our modern Cenozoic era). The time intervals of mass extinctions and superchrons (including periods of rare inversions) are shaded with vertical light and dark gray stripes, respectively.

When comparing the dependencies in Fig. 1 (a-c) it is clearly visible that four periods of superchrons (dark bands) are followed by subsequent periods of mass extinction of living beings on Earth (light gray bands), and during the 2nd, 3rd, and 4th extinctions, the relative content of oxygen molecules in the atmosphere steadily decreases. Is it possible to conclude based on this that the change in polarity (inversion) of the geomagnetic field is connected with the decrease in oxygen concentration in the Earth's atmosphere and the subsequent mass extinction of different species of living organisms on Earth? Below are the results of a study aimed at estimating the impact of both long-term and relatively rapid magnetic inversions on the composition of the Earth's atmosphere, which in turn affects the diversity of biological species.

Fig. 1.

(a) — frequency of geomagnetic inversions in the Phanerozoic era and their modeled values (dotted), for which data are missing [5]. (b) — percentage ratio and mass of atmospheric oxygen O_2 [7]; (c) — secular changes in nitrogen isotope ratios $\delta^{15}N$ with a mean value of +2.0±0.3 ‰ (dotted line) [8]. The average long-term trend is represented by a black curve and the area of uncertainty around it. The symbol δ expresses the change in isotope ratios between a sample and a standard: $\delta X = (R_{sample} / R_{standard} - 1) \cdot 1000‰$, where R is the ratio of heavy / light isotope of element X.

Throughout Earth's history, the mass of its atmosphere has not been constant [9]. The variability of the atmosphere is confirmed by engineering estimates of flight and thermoregulation of large dragonflies from the Late Carboniferous, which indicate that air density was much higher and changed during geological time [10, 11]. Analysis of the flight characteristics of Miocene giant birds also suggests that relatively recently, about 7 million years ago, the atmospheric density was significantly greater [12]. Changes in pO_2 (partial pressure of O_2) found in the composition of air trapped in rock salt also indicate variable atmospheric density from the Cambrian period to the Permian with significant changes in the content of both oxygen and nitrogen [13].

The dissipation of nitrogen ions was not taken into account in most atmospheric studies, as it was experimentally impossible to reliably separate N^+ from O^+ ions due to their similar masses. Statistical data on the relative contribution of N^+ to ionospheric outflow are also lacking. It is known that with increasing solar activity, the upper atmosphere becomes enriched with N^+ ions [14]. For example, observations from the *ISIS* -2 satellite showed that during the geomagnetic storm in August 1972 , the ionosphere at latitudes 55°-80° and altitude ~1400 km consisted predominantly of N^+ ions [14]. Additionally, during high solar activity and strong magnetic storms, the losses of heavy ions (O^+ and N^+) increase much more than those of H^+ ions [15, 16]. The non-thermal outflow of O^+ from the ionosphere increases by 100 times, while the non-thermal outflow of H^+ increases only by 3 times when the F10.7 flux increases by 3 times (from solar minimum to maximum) [16].

To test the hypothesis about the influence of multiple geomagnetic inversions on the loss of a significant part of the atmosphere, which likely led to mass extinctions, estimates of ionospheric losses of nitrogen N^+ and oxygen O^+ ions were made based on a developed semi-empirical model, both for the present time and at the moment of geomagnetic inversion, taking into account changes in solar wind (SW) pressure and EUV radiation during the Phanerozoic era.

SOLAR PARAMETERS

This section is dedicated to the evolution of solar parameters (solar wind pressure and EUV radiation) during the Phanerozoic era, and their influence on Earth's ionosphere and magnetosphere. EUV radiation leads to photoionization of planetary neutrals and heating of the upper atmosphere with its subsequent expansion. High EUV flux from solar flares and superflares can lead to extreme thermal or hydrodynamic dissipation of the atmosphere. To determine the dependence of radius r_{exo}, density n_{exo}, and temperature T_{exo} of the exobase (i.e., the height at which upward-moving particles experience on average one collision; variables related to the exobase are denoted by the subscript *exo*) on EUV flux, the hydrodynamic model proposed in [17] was modified.

Fig. 2. (a) — density profiles of oxygen O^+ (solid) and nitrogen N^+ (dashed) ions, (b) — temperature and (c) — height of the exobase, obtained from the theoretical model [14] similar to the GAIT model [21], under different conditions of solar EUV flux (normalized to the current average solar energy flux ~1×EUV, which represents the solar EUV energy flux ≈ 5.1 mW/m^2).

Altitude profiles of oxygen and nitrogen ion densities in the atmosphere depending on the intensity of EUV radiation (with weighting factors of 1, 3, and 4.5 compared to the current level) are shown in Fig. 2a. They can be approximated by the Chapman function for a simple ionospheric layer [18]:

$$n(h) = n_0 \exp\left\{\frac{1}{2}\left(1 - y - e^{-y}\right)\right\}, \quad y = \int_{h_0}^{h} \frac{dh'}{H(h')}. \qquad (1)$$

Here n_0 is the maximum density at the height h_0 of the F2 layer peak. The scale height $H(h) = k_B T(h) / mg$ has a linear trend at the upper boundary of the F2 layer [19], which is in good

agreement with the expected linear dependence of temperature $T(h) = T_{exo} + ah$ with a positive temperature gradient $a \equiv \partial T / \partial h$, equal to 0.31 K / km for the oxygen layer at a temperature of $T_{exo} \approx 1000$ K. This profile assumes an idealized globally averaged atmosphere in hydrostatic equilibrium and ionized by plane-parallel monochromatic EUV radiation, while neglecting Earth's magnetic field.

In Fig. 2a shows that for all considered values of EUV radiation, the density of nitrogen ions N^+ in the atmosphere is always lower than the density of O^+ ions, which is consistent with the results of [20]. The difference in their densities decreases with increasing altitude and EUV radiation level. Fig. 2b demonstrates the temperature and height of the exobase as functions of EUV flux (in units of the current EUV flux, corresponding to the solar energy flux of 5 mW/m^2). The figure shows vertical dashed lines indicating characteristic levels of EUV radiation during the X2 solar flare of 07.XI.2004, for the solar maximum in cycle 23, and the X17 solar flare of 28.X.2003. When the solar EUV flux exceeds the current one by approximately 5 times, the temperature and height of the exobase begin to rise sharply. At such a critical level of irradiation, Earth's thermosphere may experience a rapid transition from hydrostatic equilibrium to hydrodynamic dissipation (*hydrodynamic blow-off*). Modeling has shown that the transition of the thermosphere to a state of atmospheric blow-off occurs at an exobase temperature of 7000–8000 K, which is in agreement with studies [16, 21].

Solar wind (SW) is a key energy source for the planet's plasmasphere [22], but its efficiency strongly depends on the magnitude and configuration of Earth's own magnetic field. The planet's modern magnetic field, characterized by the leading Gaussian dipole coefficient $g_1^0 = 30$ μT [23], interacts with the SW to form a magnetosphere extending on average to 10 R_E (Earth radii) at the subsolar point (i.e., at the intersection of the dayside magnetopause with the Earth - Sun line) and effectively prevents direct interaction of the SW with the planet's ionosphere.

Despite disagreements about the reliability of paleomagnetic measurements, it is believed that the geomagnetic field strength during reversal decreases to 10–20% of its current strength [24, 25]. However, during the period of multiple reversals from 3.36 to 3.03 million years ago, for approximately 60 thousand. years, weak fields with intensities less than 10% dominated [26, 27]. Geodynamo models can reproduce various inversion scenarios depending on the expected behavior of the conductive fluid inside the Earth [28]. According to the model [29], the total intensity of the geomagnetic field during inversion decreases to 10%, with the quadrupole component dominating over the dipole. We neglect the dipole component and consider two cases: a quadrupole field with modern intensity of $g_2^0 = 2.5$ μT and with a tenfold reduced intensity of $g_2^0 = 0.25$ μT, as in work [6]. The average distance to the magnetopause of the quadrupole field at the subsolar point under quiet solar conditions is 3.4 R_E or 1.9 R_E for $g_2^0 = 0.25$ μT and $g_2^0 = 0.25$ μT, respectively [23]. The distance to the magnetopause is determined from the balance between the dynamic pressure of the SW $P_{sw} = m_p n_{sw} v_{sw}^2$ and the pressure of the planet's magnetic field $P_E = 2B_E^2(r) / \mu_0$ (or the thermal pressure of the ionosphere for an induced magnetosphere).

In work [6], an assessment of the evolution of solar parameters in the Phanerozoic era is provided. Since the Sun's mass loss rate ($\dot{M}$) depends on the star's age (t in billions of years) and its activity (X-ray flux F_X) as $\dot{M} \sim F_X^{1.15\pm0.20} \sim t^{-2.33\pm0.55}$, 600 million years ago, the SW with

pressure $P_{sw} \sim \dot{M} v_{sw}$ was 1.5 times denser than the modern SW with P_{sw0} [30, 31], and EUV fluxes were 1.5 times higher. However, comparison with the sun-like star 18 Scopii (HD 146233) aged 300 million years allows estimating the upper limit P_{sw} at 3.7 times higher than the current P_{sw0} .

The solar EUV flux changes by a factor of 3 in accordance with the eleven-year solar cycle (i.e., the energy flux varies in the range $2.5-8$ mW/m^2) [32] and can increase by 2.6 times during X-class solar flares [33]. The average SW pressure varies between 1.4–8 nPa without considering the influence of space weather. During the ascending phase of the solar cycle, solar activity increases and, consequently, the frequency of geomagnetic storms, during which the dynamic pressure of the SW can reach 50–100 nPa.

DISSIPATION MECHANISMS

In this section, we will consider the most significant mechanisms of heavy ion dissipation from Earth's atmosphere and present semi-empirical models for estimating their loss rates. The main mechanisms of atmospheric particle acceleration are shown in Table 1, summarizing the results of works [34-38]. For each mechanism, paper [39] presented loss rates of oxygen and hydrogen atoms and ions as a function of dipole magnetic field strength. Based on these estimates, the most significant mechanisms of heavy particle loss were identified. For planets with a strong intrinsic magnetic field, the greatest contribution to atmospheric losses comes from heavy ions escaping along open field lines at geomagnetic poles (corresponding to mechanism 6 in Table 1). If the intrinsic magnetic field is weaker than the induced one, the solar wind directly interacts with the ionospheric plasma and neutral gas, which facilitates ion capture and scattering. Earth's ionospheric losses caused by the solar wind were estimated in [6] and significantly exceed losses due to other mechanisms [39], which are not considered in this paper. We assume that losses of neutral atoms are less significant than losses of ionized particles.

Ions that have left the ionosphere can either immediately escape the magnetosphere or circulate within it and, ultimately, either escape into open space or return to the ionosphere. Previously, it was assumed that a significant number of oxygen ions leaving Earth through cusps and polar caps return to the atmosphere [40], but recent observations have shown that the return flows of heavy ions are insignificant [41, 42].

Table 1. Main mechanisms of planetary atmosphere dissipation [32].

No.	Mechanisms	Type	Form	Explanation
(1)	Jeans escape *(Jeans escape)*	Thermal, neutrals	H, He	Particle velocity in the high-energy tail of the distribution exceeds the escape velocity.
(2)	Hydrodynamic blow-off *(Hydrodynamic blow-off)*	Thermal, neutrals/ ions	All	Similar to the mechanism of solar wind formation (works in extreme radiation conditions)

(3)	Photochemical heating *(Photochemical heating)*	Thermochemical, chemical, neutrals	H, He	Photochemical reaction (under EUV influence) includes heating and decomposition of molecules, leading to their products escaping into space.
(4)	Ion pickup *(Ion pickup)*	Non-thermal, ions	H, He	Convection electric field $\mathbf{v}_{sw} \times \mathbf{B}_{sw}$ "picks up" excited ionospheric ions.
(5)	Secondary sputtering *(Secondary sputtering)*	Non-thermal, neutrals	All	Ionospheric ions, accelerated by SW, re-impact the upper layers of the atmosphere, causing the ejection of neutrals
(6)	Excitation by EM waves and field-aligned potentials	Non-thermal, ions	All	SW energy, locally retained at low altitudes, causes electromagnetic disturbances that excite ionospheric ions.
(7)	Large-scale momentum transfer *(SW-driven escape)*	Non-thermal, ions	All	Large-scale momentum transfer from SW to planetary plasma beyond the magnetosphere boundary.

Losses from cusps and polar caps

Polar wind (we will designate it below with the index *pw*) facilitates the ejection of thermal ions from the atmosphere due to electron pressure gradients along the magnetic poles [43, 44]. When a fully or partially ionized atmosphere is in hydrostatic equilibrium in a gravitational field (g), an ambipolar electric field forms $E = -\mu g / e$ [45], where $|e|$ is the electron charge, and $\mu = \left(\sum_\alpha Z_\alpha m_\alpha n_\alpha / T_\alpha\right) / \left(\sum_\alpha Z_\alpha^2 n_\alpha / T_\alpha\right)$ is the average ion mass, determined by the sum of all charged α-type particles (ions and electrons).

Losses from the cusp (marked with the subscript *ce*) create suprathermal ions in the energy range from several hundred to thousands of electron volts. Ion heating is achieved through the dissipation of the downward Poynting flux, transferring energy from the SW to the cusp at low altitude [46].

The loss rates of ions from the polar caps and cusps are proportional to the total area of the open field line regions $S_{pc} = \Omega_{exo} r_{exo}^2$, where Ω_{exo} — is the solid angle of the polar cap (index *pc*), defined in papers [39, 23], for dipole and quadrupole magnetic configurations:

$$Q_{pw,\alpha} \sim n_{exo,\alpha} v_{exo,\alpha} S_{pc} \ , \qquad (2)$$

where the exobase density $n_{exo,\alpha} = n_\alpha(h_{exo})$ in expression (1) and velocity $v_{exo,\alpha} = \sqrt{2E(r_{exo}) / m_\alpha}$ depend on the radius $r_{exo} = h_{exo} + R_E$, which is a function of the EUV flux $r_{exo} = h_{exo} + R_E$ (Fig. 2).

For the polar wind, the energy $E = GM_{\rm E}\mu / r_{exo}$ is gravitational, where G – Newton's gravitational constant, $M_{\rm E}$ – Earth's mass.

The ion loss rate from the cusp also depends on the solar wind energy flux incident on the magnetopause, i.e., it is proportional to its cross-section $S_c = \pi r_c^2$, (defined in papers [39, 23]):

$$Q_{ce,\alpha} \sim n_{exo,\alpha} v_{exo,\alpha} S_c S_{pc} P_{sw}^{0.61}. \quad (3)$$

Additionally, the loss rate of oxygen ions O^+ increases with the growth of the solar wind dynamic pressure (index *sw*) as $Q_{pw,O} \sim P_{sw}^{0.61}$ [47].

The ion loss rates from polar caps and cusps are determined by the scaling method according to their present values for oxygen. Thus, according to estimates, the loss rates of O^+ from polar caps and cusps are, respectively $Q_{0,pw,O^+} = 8\times10^{24}$ O^+/s [44] and $Q_{0,ce,O^+} = 2\times10^{25}$ O^+/s [48]. It is assumed that these loss rates (with index 0) correspond to the present average solar EUV flux and typical SW pressure $P_{sw0} = 1.4$ nPa with density $n_{sw} = 5$ cm^{-3} and velocity $v_{sw} = 400$ km/s.

Losses caused by the solar wind

Losses from direct solar wind are estimated based on the momentum transfer from the SW to the charged particles of the planet's atmosphere. The accelerated flux of ions leaving the magnetosphere ($\Phi_{\rm E} = n_{\rm E} v_{\rm E}$) is related to the incident SW flux ($\Phi_{sw} = n_{sw} v_{sw}$) and the locally decelerated SW flux ($\Phi_{sw\rm E}$) as follows [22]:

$$\Phi_{\rm E} = \delta \frac{v_{sw} m_{sw}}{v_{\rm E} m_{\rm E}} \left(\Phi_{sw} - \frac{v_{sw\rm E}}{v_{sw}} \Phi_{sw\rm E} \right), \quad (4)$$

where v , m , n — are the velocity, mass, and density of the charged particles of the planet's atmosphere (index E), the solar wind (index *sw*), and the decelerated SW plasma (index *sw* E); $d = d_{sw} / d_{\rm E}$ defines the thickness of the momentum exchange layer [49]

$$\delta = \left(\frac{v'_{\rm E}}{v_{sw}} \right)^2 \frac{m_{\rm E} n_{\rm E}}{m_{sw} n_{sw}} \left(1 - \frac{n_{sw\rm E} v_{sw\rm E}^2}{n_{sw} v_{sw}^2} \right)^{-1}, \quad (5)$$

where the function δ depends on the ion density $n_{\rm E} = n_{\rm E}(F_{EUV}, P_{sw})$ in the momentum transfer region.

Currently, the Earth's atmosphere is not directly exposed to the solar wind. In the absence of observational data for estimating the loss rate in the weakened Earth's magnetic field, researchers [6] draw an analogy with Mars [22] and Venus [50]. For typical values of solar wind parameters $n_{sw} = 5$ cm^{-3} and $v_{sw} = 400$ km/s, we adopt approximate estimates of flow velocity and density: $v_{sw\rm E} = 40$ km/s and $n_{sw\rm E} = 1$ cm^{-3}. The escape velocity from Mars' gravitational field, $v_{esc} = 5$ km/s, is comparable to the flow velocity from Venus' upper ionosphere, and can be used as a parameter also suitable for Earth's upper ionosphere, i.e., $v_{\rm E} = 5$ km/s.

The ionospheric loss rate of a planet directly exposed to the solar wind can be calculated as $Q_{sw-driv} = \Phi_{\rm E} S_{mt}$, where $S_{mt} = \pi \left(R_{mlb}^2 - R_{mp}^2 \right)$ is the cross-section of the momentum transfer region (index *mt*), which lies between the mass loading boundary (index *mlb*) of the solar wind by Earth's

plasma $R_{mlb} = R_{mp} + \delta(R_{mp} - R_E - 100\,\text{км})$ and the magnetopause (index *mp*) or the induced magnetosphere boundary (index *imb*) on Earth's terminator line.

ISOTOPE FRACTIONATION

The increase in the ratio of heavy isotopes to light ones in the atmosphere is one of the signs of its accelerated dissipation. This section evaluates the efficiency of mass-based isotope fractionation (separation) for the main mechanisms of Earth's ionosphere dissipation.

Most dissipation mechanisms predominantly contribute to the removal of lighter isotopes, although there are differences in fractionation efficiency. To assess a dissipation mechanism's ability to fractionate isotopes, the fractionation coefficient f is used: when $f > 1$, heavy isotopes are preferentially removed; when $f < 1$, light isotopes are removed; when $f = 1$, no fractionation occurs [51]. The fractionation coefficient, f, is used in the Rayleigh equation, which relates the initial content of removed isotopes A_1^0 and their quantity A_1 in the remainder

$$\frac{A_1^0}{A_1} = \left(\frac{R}{R_0}\right)^{1/(1-f)}, \qquad (6)$$

where $R = A_2 / A_1$ — is the isotope ratio (for example, ^{15}N/ ^{14}N). The ratio R/R_0 determines the degree of enrichment with heavy isotopes compared to the initial value. The upper limit of heavy isotope enrichment can be estimated as $R / R_0 \le \left(1 + Qt / A_1\right)^{1-f}$, where Q — is the maximum loss rate; t — is time. For example, with $f = 0.2$ and $Qt = 0.01 A_1$, we have a change in the isotopic ratio $\delta X(‰) = (R / R_0 - 1) \cdot 1000 \le 8$ (Fig. 1c).

From relations (2)–(3), it follows that loss mechanisms from cusps and polar caps contribute to the effective removal of all isotopes, resulting in low fractionation, i.e., $f = \sqrt{m_1 / m_2} \sim 1$, where m_1 and m_2 — are the masses of light and heavy isotopes, respectively.

The efficiency of fractionation due to losses caused by SW, scattering, and ion capture depends on the structure of the upper atmosphere. For plasma in hydrostatic equilibrium with density $n_\alpha(h) = n_{exo,\alpha} \exp\left(-(h - h_{exo}) / H_\alpha\right)$ the fractionation coefficient f can be calculated as

$$f = \exp\left(-\frac{g(m_2 - m_1)(R_{imb} - R_E - h_{exo})}{k_B T_{exo}}\right), \qquad (7)$$

if the planet has its own magnetic field, then the radius of the induced magnetosphere boundary R_{imb} should be replaced with the magnetopause radius R_{mp}. Thus, these dissipation mechanisms remove lighter particles due to gravitational fractionation of isotopes in the upper atmosphere. The overall effect is an increase in the amount of heavier species in the atmosphere. This effect is known as Rayleigh distillation [38].

In Fig. 3 shows the fractionation coefficients of nitrogen isotopes ^{15}N/ ^{14}N and oxygen isotopes ^{18}O/ ^{16}O due to losses caused by solar wind, depending on the solar EUV radiation and in the absence of an intrinsic magnetic field. The figure shows that losses caused by solar wind most effectively fractionate isotopes at low EUV radiation. As this radiation increases, the ionosphere (i.e., the lower boundary of the induced magnetosphere) expands, and the isotope fractionation coefficient approaches zero. The expansion of the intrinsic magnetosphere (in the presence of an intrinsic magnetic field) also reduces the fractionation coefficient.

Fig. 3. Fractionation (separation) coefficient of nitrogen isotopes (dashed) and oxygen isotopes (solid) due to losses caused by solar wind, depending on EUV flux (at solar wind pressure P_{sw0} = 1.4 nPa and in the absence of an intrinsic magnetic field B_{Tot} = 0 μT).

RESULTS

Fig. 4a shows the contribution of each dissipation mechanism to the loss rates of O^+ and N^+ ions depending on the solar EUV flux for a quadrupole magnetic field with $g_2^0 = 2.5$ μT and at a solar wind pressure of 1.4 nPa. At low EUV flux, the intrinsic magnetic field with $g_2^0 = 2.5$ μT deflects the solar wind and contributes to losses from cusps and polar caps. As EUV radiation increases, the ionosphere expands, increasing the radius of the induced magnetosphere, whose lower boundary is limited by the ionopause. When the ionosphere is directly exposed to solar wind, i.e. $R_{imb} \geq R_{mp}$, (vertical dashed line in Fig. 4a), the dominant ion dissipation mechanism changes, leading to strong isotope fractionation, and oxygen and nitrogen loss rates increase by 4-5 orders of magnitude, while the gap between N^+ and O^+ loss rates narrows as the EUV flux increases.

Fig. 4. Loss rates of oxygen O^+ ions (solid) and nitrogen N^+ ions (dashed) depending on the solar EUV flux: (a) - contribution of each dissipation mechanism for a quadrupole magnetic field with $g_2^0 = 2.5$ μT and at SW pressure of 1.4 nPa; (b, c) - total loss rates of O^+ and N^+ for various magnetic field strengths and configurations at 1.4 nPa and 30 nPa.

Fig. 4b,c shows the total loss rates of O^+ and N^+ depending on the EUV flux for the modern magnetic field with $g_1^0 = 30$ μT (thin curves) and at the moment of inversion with $g_2^0 = 2.5$ μT (thick curves) and $g_2^0 = 0.25$ μT (dashed curves) at SW pressure of 1.4 nPa (b) and 30 nPa (c). The figure shows that a weak magnetic field as well as high SW pressure increase ionospheric losses.

Figure 5 demonstrates the total loss rates of O^+ and N^+ for a quadrupole magnetic field with $g_2^0 = 2.5$ μT (thin curves) and $g_2^0 = 0.25$ μT (thick curves) during inversion depending on SW pressure at different levels of EUV radiation. In the case of low EUV radiation (1.5 times higher than present), the intrinsic magnetic field provides outflow of heavy ions from the polar caps and cusps for all considered SW pressure values at $g_2^0 = 2.5$ μT and for SW pressure values less than 30 nPa at $g_2^0 = 0.25$ μT. At high EUV radiation (4.5 times higher than present), the magnetic field cannot protect the ionosphere from direct SW impact, leading to significant ion losses even at low SW pressure.

Fig. 5. Loss rates of oxygen O^+ ions (solid) and nitrogen N^+ ions (dashed) for a quadrupole magnetic field with $g_2^0 = 2.5$ μT (thin) and $g_2^0 = 0.25$ μT (thick) depending on SW pressure.

According to Table 2, a significant part of the atmosphere can be lost in 1 million years either in a very weak magnetic field ($g_2^0 = 0.25$ μT), or in a strong magnetic field ($g_2^0 = 2.5$ μT), but in extreme solar conditions ($P_{sw} \geq 30$ nPa and 4.5×EUV-flux). Moreover, about 20% of all atmospheric losses will be nitrogen ^{14}N. A magnetic field with a strength of about 10% of its current value effectively protects the atmosphere from erosion by the solar wind under moderate solar conditions, which is consistent with the conclusion in the paper [23]. Thus, significant losses of oxygen and nitrogen require higher solar activity or lower magnetic field strength, as proposed in the paper [6]. The presented dissipation mechanism and quantitative assessment of losses over geological time can justify significant changes in atmospheric mass and atmospheric pressure.

Table 2. Total loss rates $\sum_{\alpha=O,N} m_\alpha Q_\alpha$, ratio of loss rates Q_N / Q_O and percentage of atmosphere lost in 1 million years for a dipole magnetic field with $g_1^0 = 30$ μT (currently) and quadrupole field with $g_2^0 = 2.5$ μT and $g_2^0 = 0.25$ μT (at the moment of inversion) under various solar conditions.

Gauss coeff., μT	Modern EUV	P_{sw}, nPa	$\sum_{O,N} m_\alpha Q_\alpha$, kg/s	Q_N / Q_O	Atmos. losses, % / million years)
Dip. $g_1^0 = 30$	×3	10	3.1	0.08	$1.9 \cdot 10^{-3}$
Quadrup. $g_2^0 = 2.5$	×3	10	1.5	0.08	$9.3 \cdot 10^{-4}$
Quadrup. $g_2^0 = 0.25$	×3	10	14	0.13	$8.8 \cdot 10^{-3}$
Dip. $g_1^0 = 30$	×4.5	30	16	0.15	0.01
Quadrup. $g_2^0 = 2.5$	×4.5	30	$1.1 \cdot 10^3$	0.23	0.7
Quadrup. $g_2^0 = 0.25$	×4.5	30	$2.2 \cdot 10^4$	0.19	13.4

CONCLUSIONS

In the modern Earth's dipole field with $g_1^0 = 30$ μT, oxygen losses are about 3×10^{25} O^+/s, which is an insignificant rate. According to estimates [36], the total atmospheric losses are about

1 kg/s or less. During a reversal, the geomagnetic field strength decreases to 10% or less of its current value. This reduces the magnetosphere by about two-thirds and, with strong EUV radiation, allows the solar wind to reach the ionosphere level. During solar events, EUV flux and solar wind pressure can significantly increase, resulting in a loss of 16 kg/s in the modern magnetic field with $g_1^0 = 30$ μT or a loss of $(1.1 \div 22) \times 10^3$ kg/s in weaker magnetic fields with $g_2^0 = 2.50 \div 0.25$ μT, respectively. Also, during solar events, the Earth's upper atmosphere is enriched with nitrogen ions N^+. Light nitrogen isotopes ^{14}N are more easily captured by the solar wind than oxygen isotopes, which may lead to an increase in the background of heavy nitrogen isotopes ^{15}N during geomagnetic reversals. The general conclusion from the analysis: during very long periods of multiple reversals and weak magnetic fields lasting millions of years, the mass loss of the atmosphere can have a serious impact on the biosphere.

FUNDING

This work was supported by grant No. MK-5053.2022.6 from the Ministry of Science and Higher Education of the Russian Federation.

REFERENCES

1 . *Sepkoski J.J.* Phanerozoic Overview of Mass Extinction // Patterns and Processes in the History of Life. 1986. P. 277–295. DOI: 10.1007/978-3-642-70831-2_15

2 . *Keller G.* Impacts, volcanism and mass extinction: random coincidence or cause and effect? // Australian J. Earth Sciences. 2005. V. 52 Iss. 4-5. P. 725–757. DOI: 10.1080/08120090500170393

3 . *Raup D.M., Sepkoski J.J.* Mass Extinctions in the Marine Fossil Record // Science. 1982. V. 215. Iss. 4539. P. 1501–1503. DOI: 10.1126/science.215.4539.1501

4 . *Valet J.-P., Fournier A.* Deciphering records of geomagnetic reversals // Reviews of Geophysics. 2016. V. 54. Iss. 2. P. 410–446. DOI: 10.1002/2015RG000506

5 . *Hounslow M.W., Domeier M., Biggin A.J.* Subduction flux modulates the geomagnetic polarity reversal rate // Tectonophysics. 2018. Iss. 742. P. 34–49. DOI: 10.1016/j.tecto.2018.05.018

6 . *Wei Y., Pu Z., Zong Q. et al.* Oxygen escape from the Earth during geomagnetic reversals: Implications to mass extinction // Earth and Planetary Science Letters. 2014. Iss. 394. P. 94–98. DOI: 10.1016/j.epsl.2014.03.018

7 . *Berner R.A.* Phanerozoic atmospheric oxygen: New results using the GEOCARBSULF model // American J. Science. 2009. V. 309. Iss. 7. P. 603–606. DOI: 10.2475/07.2009.03

8 . *Algeo T.J., Meyers P.A., Robinson R.S. et al.* Icehouse-greenhouse variations in marine denitrification // Biogeosciences. 2014. V. 11. Iss. 4. P. 1273–1295. DOI: 10.5194/bg-11-1273-2014

9 . *Johnson B.W., Goldblatt C.* EarthN: A New Earth System Nitrogen Model // Geochemistry, Geophysics, Geosystems. 2018. V. 19. Iss. 8. P. 2516–2542. DOI: 10.1029/2017GC007392

10 . *Cannell A.E.R.* The engineering of the giant dragonflies of the Permian: revised body mass, power, air supply, thermoregulation and the role of air density // J. Exp. Biol. 2019. Iss. 221. Art.ID. jeb185405. DOI: 10.1242/jeb.185405

11 . *Cannell A., Nel A.* Paleo-air pressures and respiration of giant Odonatoptera from the Late Carboniferous to the Early Cretaceous // Palaeoentomology. 2023. V. 6. Iss. 4. DOI: 10.11646/palaeoentomology.6.4.6

12 . *Cannell A.E.R.* Too big to fly? An engineering evaluation of the fossil biology of the giant birds of the Miocene in relation to their flight limitations, constraining the minimum air pressure at about 1.3 bar // Animal Biology. 2020. V. 70. Iss. 3. P. 1–20. DOI: 10.1163/15707563-bja10001

13 . *Cannell A., Blamey N., Brand U. et al.* A revised sedimentary pyrite proxy for atmospheric oxygen in the paleozoic: Evaluation for the silurian-devonian-carboniferous period and the relationship of the results to the observed biosphere record // Earth-Science Reviews. 2022. Art. ID 104062. DOI: 10.1016/j.earscirev.2022.104062

14 . *Hoffman J.H., Dodson W.H., Lippincott C.R. et al.* Initial ion composition results from the ISIS 2 satellite // J. Geophysical Research (1896–1977). 1974. V. 79. Iss. 28. P. 4246–4251. DOI: https://doi.org/10.1029/JA079i028p04246

15 . *Chappell C.R., Olsen R.C., Green J.L. et al.* The discovery of nitrogen ions in the Earth's magnetosphere // Geophysical Research Letters. 1982. V. 9. Iss. 9. P. 937–940. DOI: 10.1029/GL009i009p00937

16 . *Cully C.M., Donovan E.F., Yau A.W. et al.* Akebono / Suprathermal Mass Spectrometer observations of low-energy ion outflow: Dependence on magnetic activity and solar wind conditions // J. Geophysical Research (Space Physics). 2003. V. 108. Iss. A2. Art.ID. 1093. DOI: 10.1029/2001JA009200

17 . *Tian F., Kasting J. F., Liu H.-L. et al.* Hydrodynamic planetary thermosphere model: 1. Response of the Earth's thermosphere to extreme solar EUV conditions and the significance of adiabatic cooling // J. Geophysical Research (Planets). 2008. V. 113. Iss. E5. Art.ID. E05008. DOI: 10.1029/2007JE002946.

18 . *Chapman S.* The absorption and dissociative or ionizing effect of monochromatic radiation in an atmosphere on a rotating Earth part II. grazing incidence // Proc. the Physical Society. 1931. V. 43. Iss. 5. P. 483–501. DOI: 10.1088/0959-5309/43/5/302

19 . *Olivares-Pulido G., Hernández-Pajares M., Aragón- Angel A. et al.* A linear scale height Chapman model supported by GNSS occultation measurements // J. Geophysical Research (Space Physics). 2016. V. 121. Iss. 8. P. 7932–7940. DOI: 10.1002/2016JA022337

20 . *Tian F., Solomon S.C., Qian L. et al.* Hydrodynamic planetary thermosphere model: 2. coupling of an electron transport/energy deposition model // J. Geophysical Research: Planets. 2008. V. 113. Iss. E7. DOI: 10.1029/2007JE003043

21 . *Smithtro C.G., Sojka J.J.* Behavior of the ionosphere and thermosphere subject to extreme solar cycle conditions // J. Geophysical Research (Space Physics). 2005. V. 110. Iss. A8. Art.ID. A08306. DOI: 10.1029/2004JA010782

22 . *Lundin R., Dubinin E.M.* Phobos-2 results on the ionospheric plasma escape from Mars // Advances in Space Research. 1992. Iss. 12. P. 255–263. DOI: 10.1016/0273-1177(92)90338-X

23. *Tsareva O.O., Dubinin E.M., Malova H.V. et al.* Atmospheric escape from the earth during geomagnetic reversal // Ann. Geophys. 2019. V. 63. Iss. 2. Art.ID PA223. DOI: 10.4401/ag-8354

24 . *Merrill R.T., McFadden P.L.* Paleomagnetism and the nature of the geodynamo // Science. 1990. V. 248. Iss. 4953. P. 345–350. DOI: 10.1126/science.248.4953.345

25 . *Leonhardt R., Fabian K.* Paleomagnetic reconstruction of the global geomagnetic field evolution during the matuyama/brunhes transition // Earth and Planetary Science Letters. 2007. Iss. 253. P. 172–195. DOI: 10.1016/j.epsl.2006.10.025

26 . *Valet J.-P., Thevarasan A., Bassinot F. et al.* Two records of relative paleointensity for the past 4 Myr. // Frontiers in Earth Science. 2020. V. 8. Art.ID 148. DOI: 10.3389/feart.2020.00148

27 . *Herrero-Bervera E., Valet J.-P.* Absolute paleointensity and reversal records from the Waianae sequence (Oahu, Hawaii, USA) // Earth and Planetary Science Letters. 2005. V. 234. Iss. 1–2. P. 279–296. DOI: 10.1016/j.epsl.2005.02.032

28 . *Jacobs J.A.* Reversals of the Earth's magnetic field. 2 nd edition. Cambridge: Cambridge Univ. Press, 1994.

29 . *Glatzmaier G.A., Roberts P.H.* A three-dimensional self-consistent computer simulation of a geomagnetic field reversal // Nature. 1995. V. 377. Iss. 6546. P. 203–209. DOI: 10.1038/377203a0

30 . *Wood B.E., Muller H.-R., Zank G.P. et al.* Measured mass-loss rates of solar-like stars as a function of age and activity // The Astrophysical J. 2002. V. 574. Iss. 1. P. 412–425. DOI: 10.1086/340797

31 . *Güdel M., Kasting J.* Origins and evolution of life: The young sun and its influence on planetary atmospheres. Cambridge: Cambridge University Press, 2011 .

32 . *Mansoori A., Khan P., Ahmad R. et al.* Evaluation of long term solar activity effects on GPS derived tec. // J. Physics: Conference Series. 2016. V. 759. Art.ID 012069. DOI: 10.1088/1742-6596/759/1/012069

33 . *Krauss S., Pfleger M., Lammer H.* Satellite-based analysis of thermosphere response to extreme solar flares // Annales Geophysicae. 2014. V. 32. Iss. 10. P. 1305–1309. DOI: 10.5194/angeo-32-1305-2014

34 . *Yamauchi M., Wahlund J.-E.* Role of the Ionosphere for the Atmospheric Evolution of Planets // Astrobiology. 2007. V. 7. Iss. 5. P. 783–800. DOI: 10.1089/ast.2007.0140

35 . *Lundin R., Dubinin E.M., Koskinen H. et al.* On the momentum transfer of the solar wind to the Martian topside ionosphere // Geophysical Research Letters. 1991. V. 18. Iss. 6. P. 1059–1062. DOI: 10.1029/90GL02604

36 . *Lundin R., Lammer H., Ribas I.* Planetary magnetic fields and solar forcing: Implications for atmospheric evolution // Space Science Reviews. 2007. V. 129. Iss. 1–3. P. 245–278. DOI: 10.1007/s11214-007-9176-4

37 . *Brain D.A., Bagenal F., Ma Y.-J., et al.* Atmospheric escape from unmagnetized bodies // J. Geophys. Res. Planets. 2016. V. 121. DOI: 10.1002/2016JE005162

38. *Gronoff G., Arras P., Baraka S. et al.* Atmospheric escape processes and planetary atmospheric evolution: from misconceptions to challenges // Proc. European planetary science congress. 2020. EPSC2020-32. DOI: 10.5194/epsc2020-32

39 . *Gunell H., Maggiolo R., Nilsson H. et al.* Why an intrinsic magnetic field does not protect a planet against atmospheric escape // Astronomy and Astrophysics. 2018. V. 614. Iss. L3. DOI: 10.1051/0004-6361/201832934

40 . *Seki K., Elphic R.C., Hirahara M. et al.* On atmospheric loss of oxygen ions from Earth through magnetospheric processes // Science. 2001. V. 291. Iss. 5510. P. 1939–1941. DOI: 10.1126/science.1058913

41 . *Slapak R., Hamrin M., Pitkänen T. et al.* Quantification of the total ion transport in the near-Earth plasma sheet // Annales Geophysicae. 2017. V. 35. Iss. 4. P. 869–877. DOI: 10.5194/angeo-35-869-2017

42 . *Slapak R., Schillings A., Nilsson H. et al.* Atmospheric loss from the dayside open polar region and its dependence on geomagnetic activity: implications for atmospheric escape on

evolutionary timescales // Annales Geophysicae. 2017. V. 35. Iss. 3. P. 721–731. DOI: 10.5194/angeo-35-721-2017

43 . *Banks P.M., Holzer T.E.* The polar wind // J. Geophysical Research. 1968. V. 73. Iss. 21. P. 6846–6854. DOI: 10.1029/JA073i021p06846

44 . *Yau A.W., Abe T., Peterson W.K.* The polar wind: Recent observations // J. Atmospheric and Solar-Terrestrial Physics. 2007. V. 69. Iss. 16. P. 1936–1983. DOI: 10.1016/j.jastp.2007.08.010

45. *Pierrard V., Lemaire J.* Lorentzian ion exosphere model // J. Geophysical Research. 1996. V. 101. Iss. A4. P. 7923–7934. DOI: 10.1029/95JA03802

46 . *Strangeway R.J., Ergun R.E., Su Y.-J. et al.* Factors controlling ionospheric outflows as observed at intermediate altitudes // J. Geophysical Research (Space Physics). 2005. Iss. 110. Art.ID A03221. DOI: 10.1029/2004ja010829

47 . *Fok M.-C., Ebihara Y., Moore T.E.* Inner magnetospheric plasma interaction and coupling with the ionosphere // Adv. Polar Upper Atmos. Res. 2005. V. 19. P. 106–134.

48 . *Pollock C.J., Chandler M.O., Moore T.E. et al.* A survey of upwelling ion event characteristics // J. Geophys. Res. 1990. V. 95. Iss. A11. P. 18969–18980. DOI: 10.1029/JA095iA11p18969

49 . *Perez-de-Tejada H.* Momentum transport in the solar wind erosion of the Mars ionosphere // J. Geophysical Research: Planets. 1998. Iss. 103. P. 31499–31508. DOI: 10.1029/1998JE900001

50 . *Perez-de-Tejada H.* Solar wind-driven plasma flows in the Venus and Mars ionospheres // Advances in Space Research. 1992. V. 12. Iss. 9. P. 265–274. DOI: 10.1016/0273-1177(92)90339-Y

51 . *Lammer H., Scherf M., Kurokawa H. et al.* Loss and fractionation of noble gas isotopes and moderately volatile elements from planetary embryos and early Venus, Earth and Mars // Space Science Reviews. 2020. V. 216. Iss. 4. Art.ID. 74. DOI: 10.1007/s11214-020-00701-x

FIGURE CAPTIONS FOR THE ARTICLE

Fig. 1. (a) — frequency of geomagnetic inversions in the Phanerozoic era and their modeled values (dotted), for which data are absent [5]. (b) — percentage ratio and mass of atmospheric oxygen O2 [7]; (c) — secular changes in nitrogen isotope ratios δ15N with a mean value of +2.0±0.3 ‰ (dotted line) [8]. The average long-term trend is represented by a black curve and the uncertainty area around it. The symbol δ expresses the change in isotope ratios between the sample and the standard: $dX = (R_{sample} / R_{standard} - 1) \times 1000‰$, where R is the ratio of heavy/light isotopes of element X.

Fig. 2. (a) — density profiles of oxygen ions O^+ (solid) and nitrogen N^+ (dotted), (b) — temperature and (c) — exobase height, obtained from a theoretical model [14] similar to the GAIT model [21], under various conditions of solar EUV flux (normalized to the current average solar energy flux ~1×EUV, which represents the solar energy EUV flux $\approx$ 5.1 mW/m^2).

Fig. 3. Fractionation coefficient (separation) of nitrogen isotopes (dotted) and oxygen (solid) due to losses caused by SW, depending on the EUV flux (at SW pressure P_{sw0} = 1.4 nPa and in the absence of an intrinsic magnetic field B_{Tot} = 0 μT).

Fig. 4. Loss rates of oxygen O^+ ions (solid) and nitrogen N^+ ions (dotted) as a function of solar EUV flux: (a) — contribution of each dissipation mechanism for quadrupole magnetic field with $g_2^0 = 2.5$ μT and solar wind pressure of 1.4 nPa; (b, c) — total loss rates of O^+ and N^+ for different magnetic field strengths and configurations at 1.4 nPa and 30 nPa.

Fig. 5. Loss rates of oxygen O^+ ions (solid) and nitrogen N^+ ions (dotted) for quadrupole magnetic field with $g_2^0 = 2.5$ μT (thin) and $g_2^0 = 0.25$ μT (thick) as a function of solar wind pressure.

FIGURES

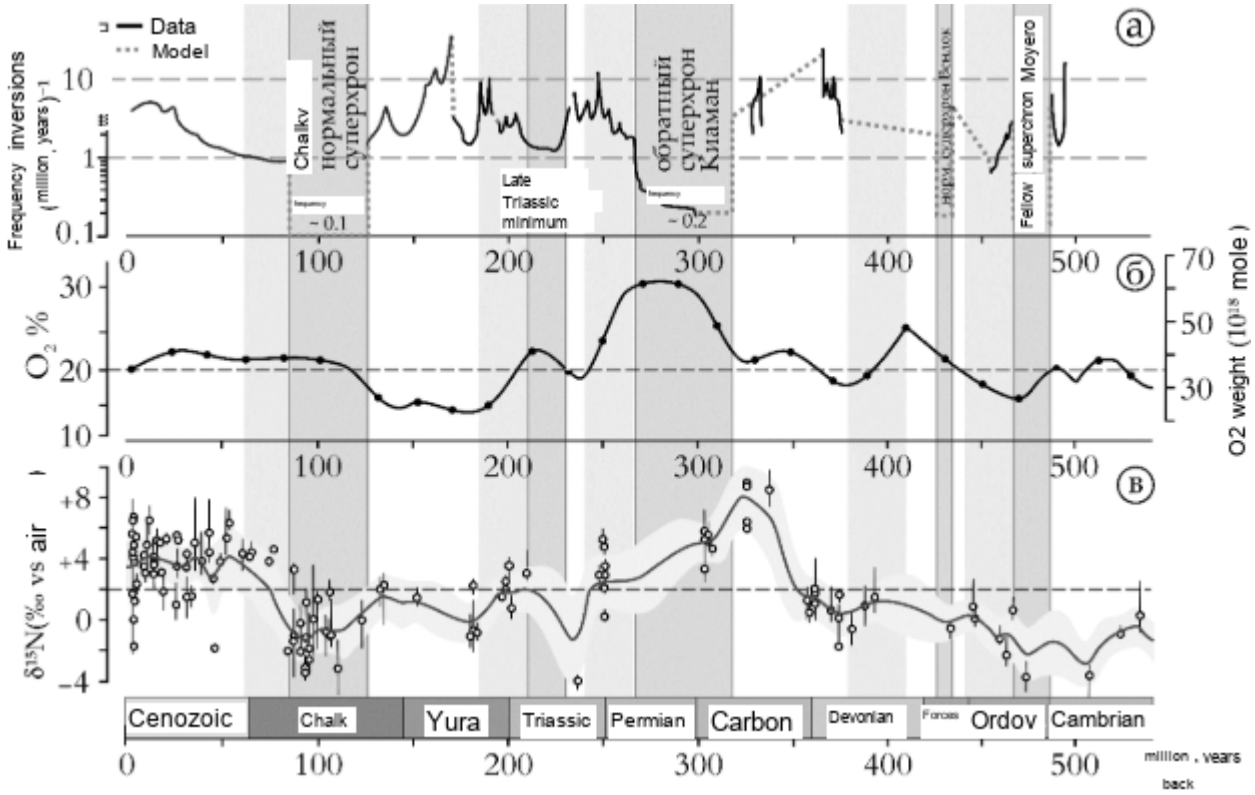

Fig. 1. Tsareva

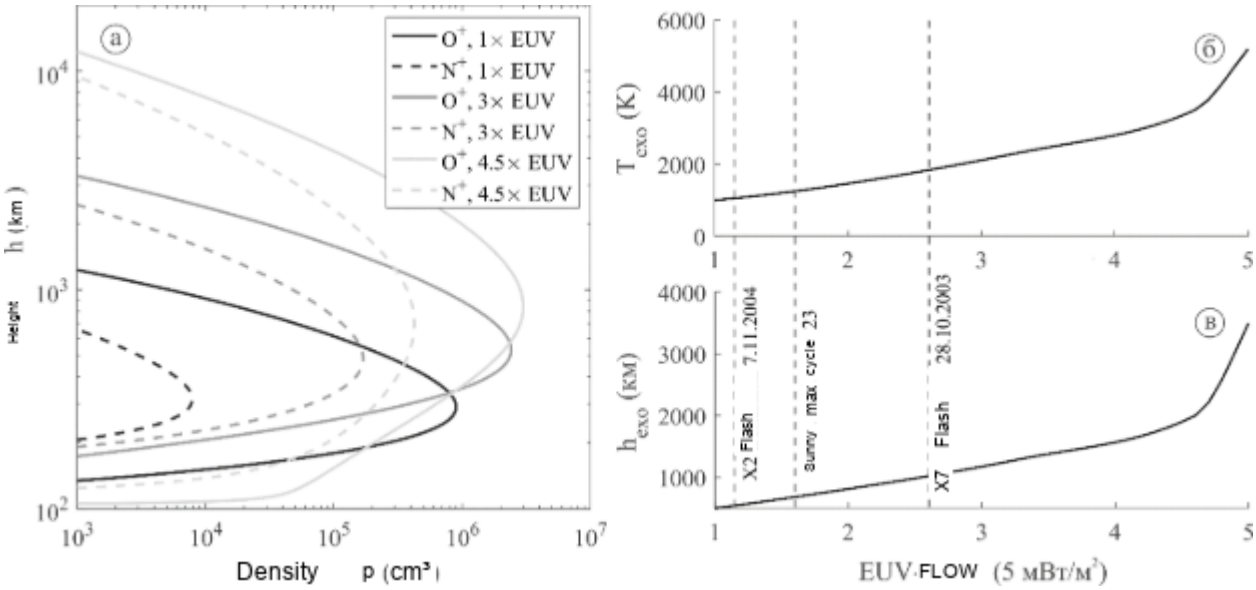

Fig. 2. Tsareva

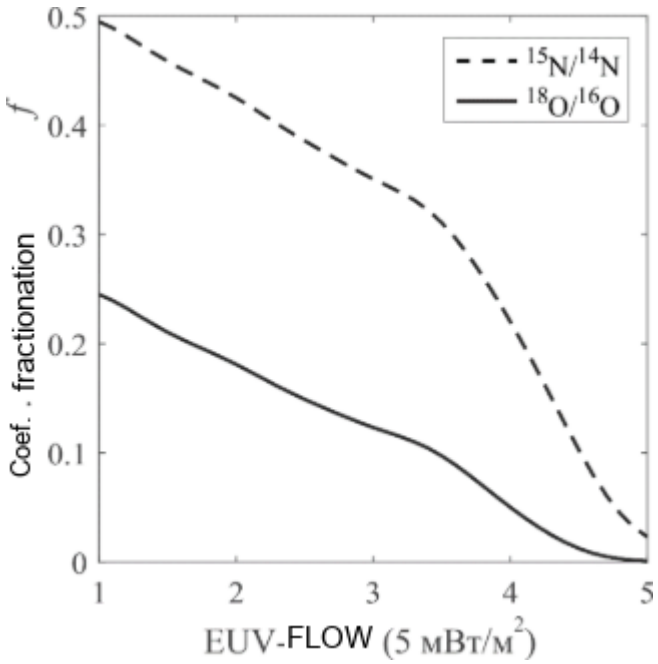

Fig. 3. Tsareva

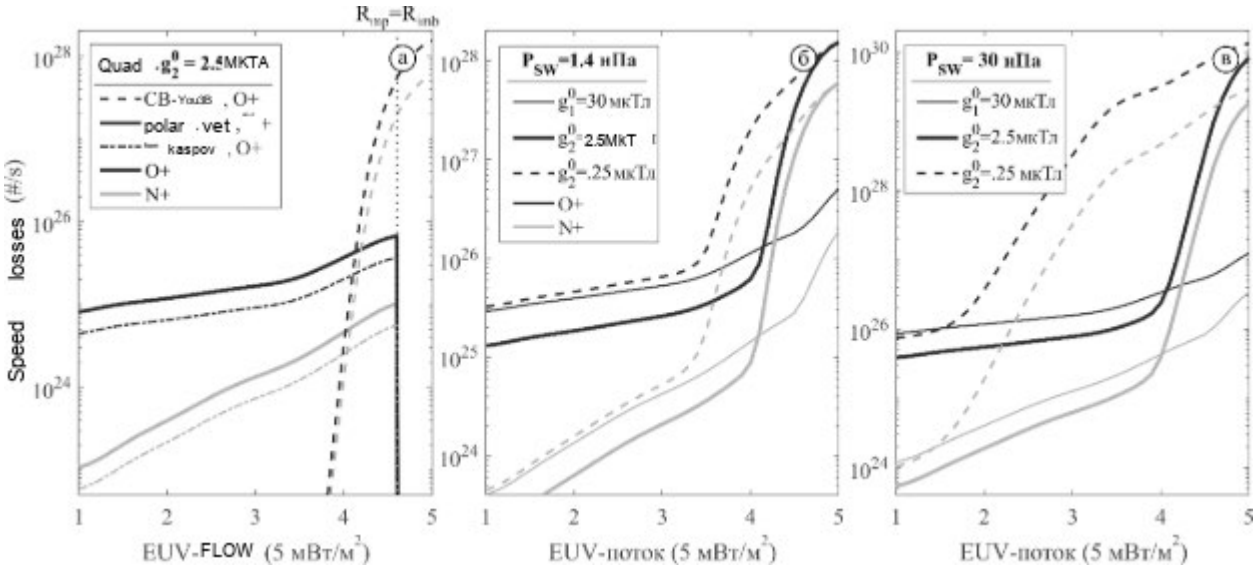

Fig. 4. Tsareva

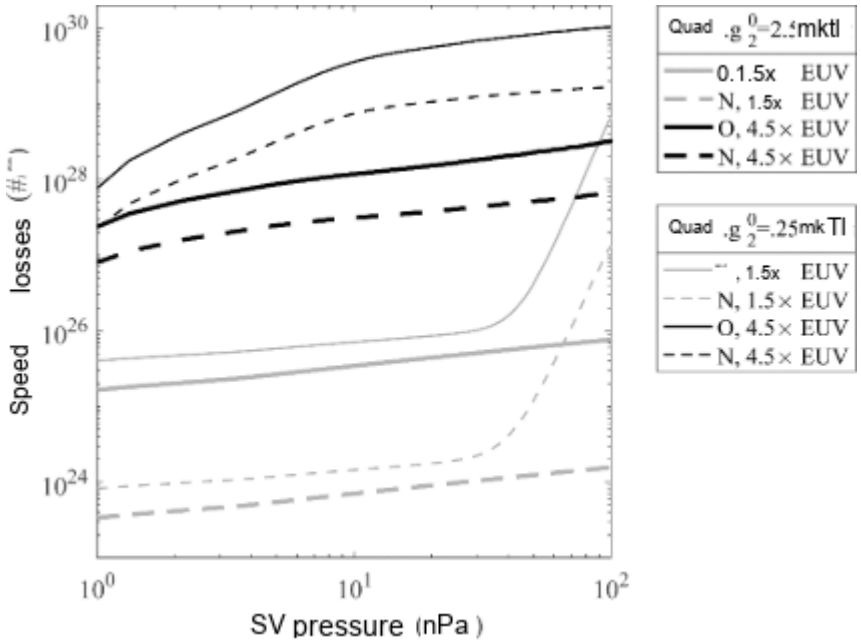

Fig. 5. Tsareva